Available online at www.sciencedirect.com
ScienceDirect
Journal of Nuclear Materials 371 (2007) 161–170
journal of nuclear materials
www.elsevier.com/locate/jnucmat

# Corrosion behavior of a ferritic/martensitic steel HCM12A exposed to harsh environments

L. Tan *, M.T. Machut, K. Sridharan, T.R. Allen

*Department of Engineering Physics, University of Wisconsin-Madison, 1500 Engineering Drive, Madison, WI 53706, USA*

**Abstract**

The corrosion behavior of a 12%Cr ferritic/martensitic steel, HCM12A, exposed separately in supercritical water (SCW) and lead–bismuth eutectic (LBE) was evaluated focusing on the microstructure of the corrosion products that develops in the first 333–1000 h. The effect of an yttrium-coating layer on the corrosion resistance of the steel was also studied. Detailed comparison of the corrosion results, including oxide scale layer structure, oxide grain morphology, texture development, and distribution of phases and alloying elements, between as-heat treated and Y-coated samples, and between SCW- and LBE-exposed environments, are reported. Scanning electron microscopy/energy dispersive X-ray spectroscopy (SEM/EDS), X-ray diffractometry (XRD), and electron backscatter diffraction (EBSD) were employed for these analyses. The outer oxide scale, magnetite, was detached/dissolved into LBE but not in SCW. Exposure results indicate that the Y-coating improved the corrosion resistance, as represented by a smaller weight gain, thinner oxide scale, and prevention of the oxide scale from detachment into LBE compared as compared to that which occurred on the non-Y treated samples.


## 1. Introduction

With the rapid increase in the demand for energy, it is indispensable to develop nuclear energy as one of the prominent energy supplies. A new generation of innovative nuclear energy systems known as Generation IV is now under development for enhancing their future role. The supercritical-water-cooled reactor system (SCWR) and lead-cooled fast reactor system (LFR) are two among the concepts selected for the Generation IV systems. The SCWR operates above the thermodynamic critical point of water (22.1 MPa, 374 °C), resulting in improved economics with high thermal efficiency. The LFR employs a long-life core cooled with liquid lead or lead–bismuth eutectic (LBE), leading to improved proliferation resistance and physical protection. A significant challenge facing the SCWR and the LFR is the selection and development of structural and cladding materials suitable for long-term use in such highly corrosive environments. Corrosion in these environments can manifest itself in several forms including dissolution such as Ni in lead [1], compound formation, and liquid metal penetration along grain boundaries (for the LFR) [2]. Several factors contribute to the corrosion mechanisms:

* Corresponding author. Tel.: +1 608 262 7476; fax: +1 608 263 7451.
*E-mail address:* lizhentan@wisc.edu (L. Tan).

0022-3115/$ - see front matter © 2007 Elsevier B.V. All rights reserved.
doi:10.1016/j.jnucmat.2007.05.001

temperature and thermal gradient, exposure time, flow rate, material compositions, and coolant chemistry, in particular its oxygen content.

Ferritic/martensitic (F/M) steels have been widely studied and developed for applications in the energy industry. The performance of FM steels in various energy systems has been reviewed by Klueh and Harries [3]. In this alloy family, alloy HCM12A (12Cr–2W–0.4Mo–1Cu–V, Nb) is one of the third generation 12Cr ferritic steels with tempered martensite [4], which was originally developed for heavy section components such as headers and steam pipes for use at temperatures up to 620 °C and pressures up to 34 MPa [5] with good resistance to thermal shocks [6]. HCM12A is one of the leading candidate F/M steels for Generation IV systems, e.g., SCWR and LFR (as well as the sodium-cooled fast reactor), due to its high strength and favorable corrosion resistance. To be employed in these harsh environments, materials' performance is critical. The performance of HCM12A exposed to steam in subcritical water indicated a parabolic growth rate of duplex oxide scales consisting of a Cr-free outer layer (magnetite) and a Cr-rich inner layer (spinel) [7,8]. Preliminary result on the performance of HCM12A exposed to SCW at 500 °C and 25 MPa with a ~25 ppb dissolved oxygen concentration lead to a similar result without noticeable exfoliation [9]. The study of the performance of HCM12A exposed in LBE containing $10^{-6}$ wt% of oxygen at temperatures <550 °C indicates good resistance against corrosion by the formation of spinel layer on the base metals, though the outer porous oxide formed on the steels was detached and/or dissolved into LBE [10]. At temperatures above 600 °C, the oxide layer thickness diminished with increasing temperature due to the formation of wustite in an environment with favorable oxygen partial pressure [10].

Although limited results on the corrosion behavior of HCM12A exposed in SCW and LBE have been reported so far, systematic comparison on the corrosion induced by SCW and LBE has not yet been performed. In the present study, the corrosion behavior of HCM12A exposed in SCW and LBE is evaluated and compared focusing on the microstructure of the corrosion products. In addition, the beneficial effect of Y additives against high-temperature oxidation has been recognized for many years [11] due to its propensity to form a very stable oxide, but the knowledge on its effect on an alloy's corrosion in SCW is limited. The effectiveness of a thin coating layer of yttrium on the corrosion resistance of HCM12A exposed to SCW and LBE was tested and the results are reported here.

## 2. Experiments

The material, HCM12A, used in this study was procured from Sumitomo Metal Industries, Ltd. with composition (wt%) provided by the supplier: 10.83Cr, 1.89W, 1.02Cu, 0.64Mn, 0.39Ni, 0.30Mo, 0.27Si, 0.19V, 0.11C, 0.063N, 0.054Nb, 0.016P, 0.002S, 0.001Al, $3.1 \times 10^{-5}$ B, and Fe as balance. The HCM12A was received after being annealed at 1050 °C and tempered at 770 °C. Rectangular samples were cut from the as-received alloy and polished to 1 μm surface finish. SCW and LBE exposure tests were performed in the University of Wisconsin SCW loop and the Los Alamos National Laboratory LBE development of lead-alloy technologies and applications (DELTA) loop, respectively. The detailed construction and system capabilities of this SCW loop are described in Refs. [12,13]. The samples and test conditions are listed in Table 1. In both cases, the oxygen was continuously refreshed during the test. The 10 ppb O in the Pb–Bi was measured using a solid state YSZ oxygen sensor with a $Bi/Bi_2O_3$ reference test section heaters were slowly ramped down after the exposure test. The corrosion behavior of the samples was characterized by means of gravimetry, scanning electron microscopy/energy dispersive X-ray spectroscopy (SEM/EDS), X-ray diffractometry (XRD), and electron backscatter diffraction (EBSD).

An electronic balance with an accuracy of 0.1 mg was used for the measurement of weight change of SCW-exposed samples. The weight change of samples exposed in LBE was not measured due to the difficulty in keeping the oxide scale intact during removal of the attached Pb–Bi alloy and the high relative error that excess Pb–Bi left on surfaces would produce.

The corrosion phenomena of SCW- and LBE-exposed samples were analyzed using a LEO 1530 field-emission SEM integrated with EDS. Corrosion products on the exposed samples were protected by a deposited Ta-coating layer for preparing cross-section samples. To obtain good quality EBSD patterns, the cross-section samples were polished with SiC abrasive paper to 1200 grit followed by diamond paste, alpha alumina, and colloidal silica solutions in sequence. The EBSD analysis was

Table 1
Samples and test conditions of SCW and LBE exposures

| Test | Sample | $T$ (°C) | Pressure (MPa) | Oxygen (ppb) | Flow (m/s) | Time (h) |
|---|---|---|---|---|---|---|
| SCW | AR<br>Y | ~600 | ~25 | ~25 | ~1 | 333, 667, 1000 |
| LBE | AR<br>Y | ~530 | N/A | ~10 | ~1.2 | 600 |

*Note*: AR, as-received samples (normalized at 1050 °C and tempered at 770 °C); Y, samples coated with yttrium via sputtering deposition followed by $Xe^+$ bombardment to improve the adhesion between the coating layer and the matrix (effective thickness ~0.3 μm).

performed on a LEO 1530 FEGSEM incorporated with a TSL orientation imaging microscopy (OIM) system MSC2200. The SEM was operated at 20 kV, and the automatic EBSD area scan was performed using a hexagonal grid with a step size of 0.1 m. To allow identification of the existing phases with the EBSD analytical software, crystallographic data files were established based on the XRD analysis in this work in addition to the available database included in the software. For phase analysis with EBSD, a voting scheme and the confidence index (CI) established by TSL were used [14]. A high number of votes and higher CI values indicate a higher possibility that the phase is correctly identified.

## 3. Results and discussion

### 3.1. Gravimetry of SCW-exposed samples

Weight gain and oxide scale thickness of the exposed samples, which were measured using a balance and from cross-section SEM images, respectively, are shown in Fig. 1. It is clear that Y-coated samples have smaller weight gain and thinner oxide scale than as-received samples. The data of as-received and Y-coated samples approximately follow a linear function as shown in Fig. 1. An offset between the data and the fitted line may indicate the possibility of scale exfoliation, phase formation/transformation, or porosity development [7]. Data following a linear function indicate stable growth of an oxide scale formed on as-received and Y-coated samples. The weight gain of the oxide scale formed on as-received and Y-coated samples approximately follows the equations of $x^{2.19} = 0.13{\cdot}t$ ($R^2 = 0.94$) and $x^{2.54} = 0.10{\cdot}t$ ($R^2 = 0.99$), respectively, where $x$ is weight gain in mg/cm$^2$, $t$ is time in h, and $R^2$ denotes the fitting quality with 1 for a perfect confidence fit. The thickness versus time of the two types of samples possesses similar

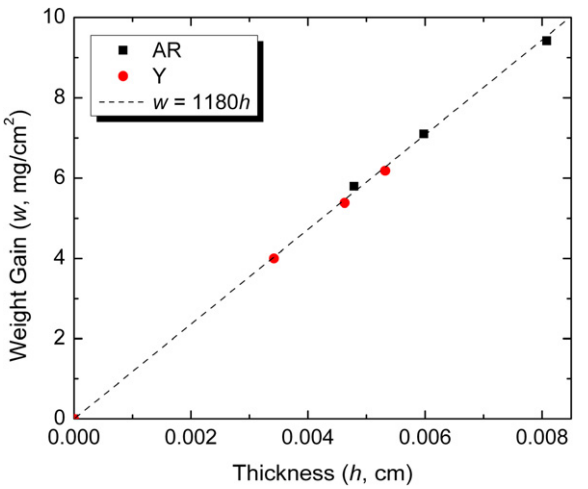


Fig. 1. Weight gain as a function of oxide scale thickness for as-received (AR) and yttrium-coated (Y) HCM12A samples exposed in SCW at 600 °C for 333, 667 and 1000 h.

functions. Thus, the oxidation of as-received samples approximately follows a parabolic rate law, while the oxidation of Y-coated samples follows a rate law between parabolic and cubic. The thin Y-coating layer decreased the rate constant of the oxidation but did not significantly alter the oxides' properties such as composition and porosity. The Y additives slowing down oxidation rate is consistent with the observation of Y in an Fe–25Cr alloy [15]. Although the oxidation kinetics provide some insight on the oxide scale behavior in a short period of time (1000 h), tests with longer exposure time are necessary to get good lifetime prediction. Since the weight gain of the samples is mainly induced by oxygen incorporated in the oxide scale, the slope of the fitted line indicates the average density of oxygen in the oxide scale, e.g., 1.18 g/cm$^3$ in Fig. 1. This oxygen density is less than the calculated average oxygen density in the oxide scale, 1.37 g/cm$^3$, based on chromite ($FeCr_2O_4$, 4.79 g/cm$^3$) and magnetite ($Fe_3O_4$, 5.15 g/cm$^3$), which implies the presence of porosity in the oxide scale.

### 3.2. Phases formed in the oxide scale on SCW-exposed samples (XRD)

XRD was performed to analyze phases created due to SCW exposure. Both as-received and Y-coated samples exposed to three different durations (333, 667, and 1000 h) possess similar XRD patterns with magnetite as the major component. The oxide scale on Y-coated samples was partially removed to ensure the analyzed regions close to the Y-coated layer (denoted as Y-int1) and the interface between the spinel and the matrix (Y-int2) were analyzed. The identified phases are listed in Table 2. The International Centre for Diffraction Data (ICDD) database were used to identify these phases such as magnetite (M, PDF [19–629]), spinel (S, PDF [34–140]) $YFeO_3$ (PDF [39–1489]), $Cr_{1.3}Fe_{0.7}O_3$ (PDF [35–1112]), and ferrite (PDF [34–396]). It is clear that the Y-coating introduced the presence of $YFeO_3$ ('Y-int1'). The presence of $Cr_{1.3}Fe_{0.7}O_3$ at 'Y-int2' also existed in as-received samples.

### 3.3. Oxide morphology of SCW-exposed samples (SEM)

The SEM plan-view images as shown in Fig. 2 exhibit oxide morphology of as-received and Y-coated samples after exposure to SCW for about 667 h. The SEM images with low magnification show some dents and humps on as-received (Fig. 2(a)) and Y-coated (Fig. 2(c)) samples, respectively. The enlarged SEM images (Fig. 2(b and d)) show faceted oxide grains, some erosion on the facets, and cracks along the boundaries of the oxide grains on both of the samples. SEM plan-view images were not acquired for LBE-exposed samples due to the adhesion of Pb–Bi on the surface.

### 3.4. Oxide layer structure (SEM/EDS)

The corrosion results of as-received samples exposed in SCW and LBE are shown in the cross-section SEM images (Fig. 3). The oxide scale on the SCW-exposed sample is mainly composed of two layers, the outer magnetite and the inner spinel. The spinel layer is slightly thinner than the magnetite layer. The sharp interface between the magnetite and the spinel is believed to be the initial surface of the sample prior to exposure. In addition to the two layers, an internal oxidation layer is present at most of the interface between the spinel and the matrix. Compared to the oxide scale formed on the SCW-exposed sample, the internal oxidation layer is a continuous layer beneath the spinel layer formed on the LBE-exposed sample. The spinel layer on the LBE-exposed sample is thinner than that on the SCW-exposed sample. The same oxide phases and layer structure formed on as-received samples exposed in both SCW and LBE environments indicate that the materials were exposed to similar thermodynamically favorable oxygen partial pressures; the different oxide layer thickness on SCW- and LBE-exposed samples indicates different oxidation kinetics induced by the exposed temperatures and oxygen partial pressures. The major difference of the oxide layer structure formed on HCM12A exposed in SCW and LBE environments is the magnetite layer. Compared to the porous magnetite layer on the SCW-exposed sample, detachment of most of the magnetite layer occurred on LBE-exposed sample, which is consistent with the literature report [10]. The detachment of the magnetite layer may be caused by the nature of the LBE flow which has dynamic pressure and shear stress on the oxide scale surface much higher than SCW because of the high density of LBE.

Detailed comparison of the SEM/EDS results of Y-coated samples exposed in SCW and LBE is shown in Fig. 4. A two-layer oxide scale, consisting of outer magnetite and inner spinel layers, was formed on the SCW-exposed sample. A light gray band in the magnetite layer close to the interface of the magnetite and the spinel is the Y-coating layer. This was confirmed by the EDS line-scan and the map of Y as shown in Fig. 4(a). The Y-spectra in the EDS line-scan of the minor elements are truncated to ensure an easier view of the other elements. Based on the XRD result ('Y-int1'), $YFeO_3$ formed at the Y-coating layer. This is reasonable since the growth of the magnetite layer is controlled by the outward diffusion of Fe. The Y-coating layer was transformed into $Y_2O_3$ due to its high affinity

Table 2
Phases present in the oxide scale of SCW-exposed as-received (AR) and Y-coated (Y) samples

| Condition | AR | Y | Y-int1 | Y-int2 |
|---|---|---|---|---|
| Phase | Magnetite | Magnetite | Magnetite (spinel), $YFeO_3$ | Spinel, ferrite, $Cr_{1.3}Fe_{0.7}O_3$ |

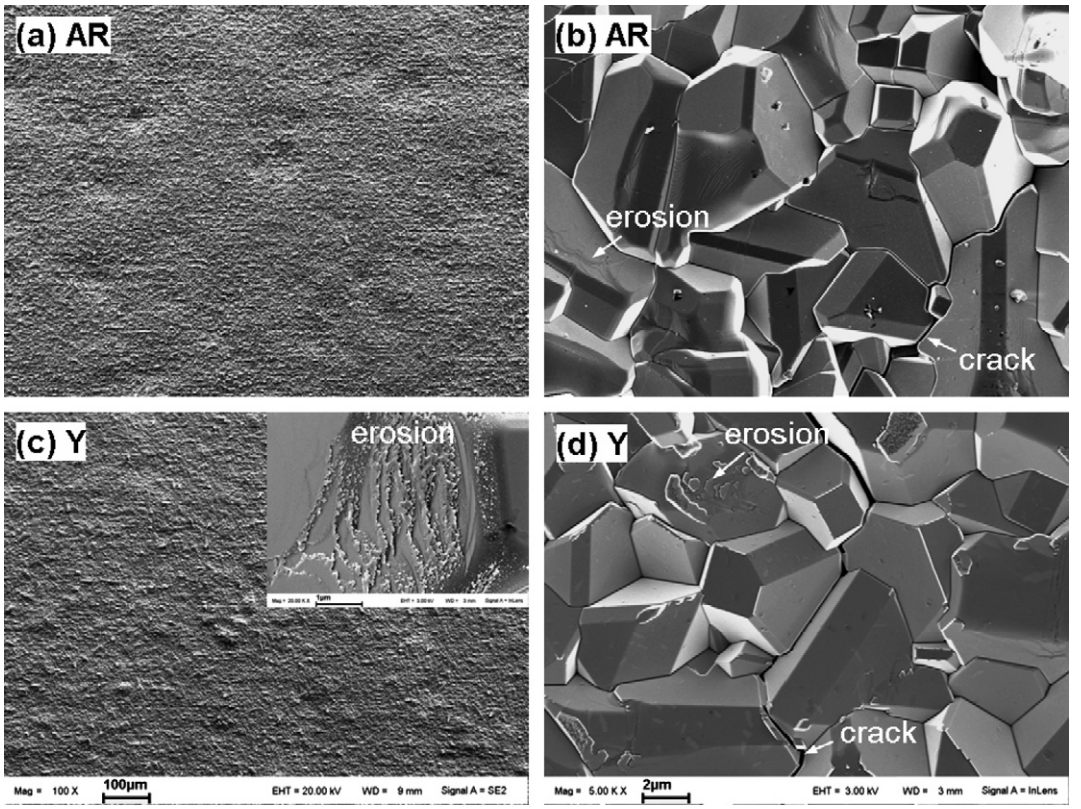


Fig. 2. Secondary electron images at different magnification of (a, b) as-received (AR) and (c, d) Y-coated (Y) samples exposed to SCW at 600 °C for 667 h. A typical erosion morphology on Y-coated samples is shown as an inset in (c).

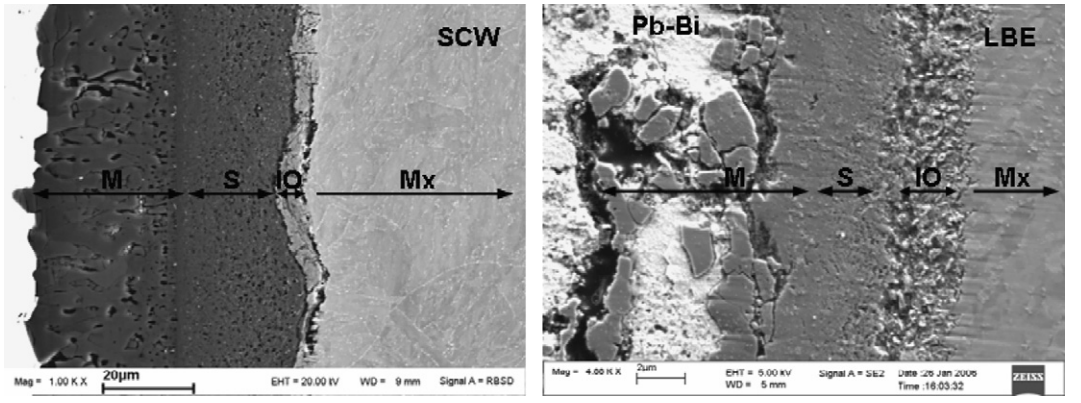


Fig. 3. Cross-section SEM images of SCW- (667 h) and LBE-exposed (600 h) as-received HCM12A samples. The labels on the images are corresponding to magnetite (M), spinel (S), internal oxidation layer (IO), and matrix (Mx).

for oxygen, and moved outwards by the Fe diffusion from its original location at the interface of the magnetite and the spinel. Some of the outward diffusing Fe ions were trapped by $Y_2O_3$ forming $YFeO_3$ due to favorable thermodynamics. The effect of the Y-coating layer on the local microstructure and species diffusion is being further studied using analytical high-resolution microscopes. The Y-coating layer separates the magnetite layer into two sublayers: a thick outer porous layer (~22 μm) and a

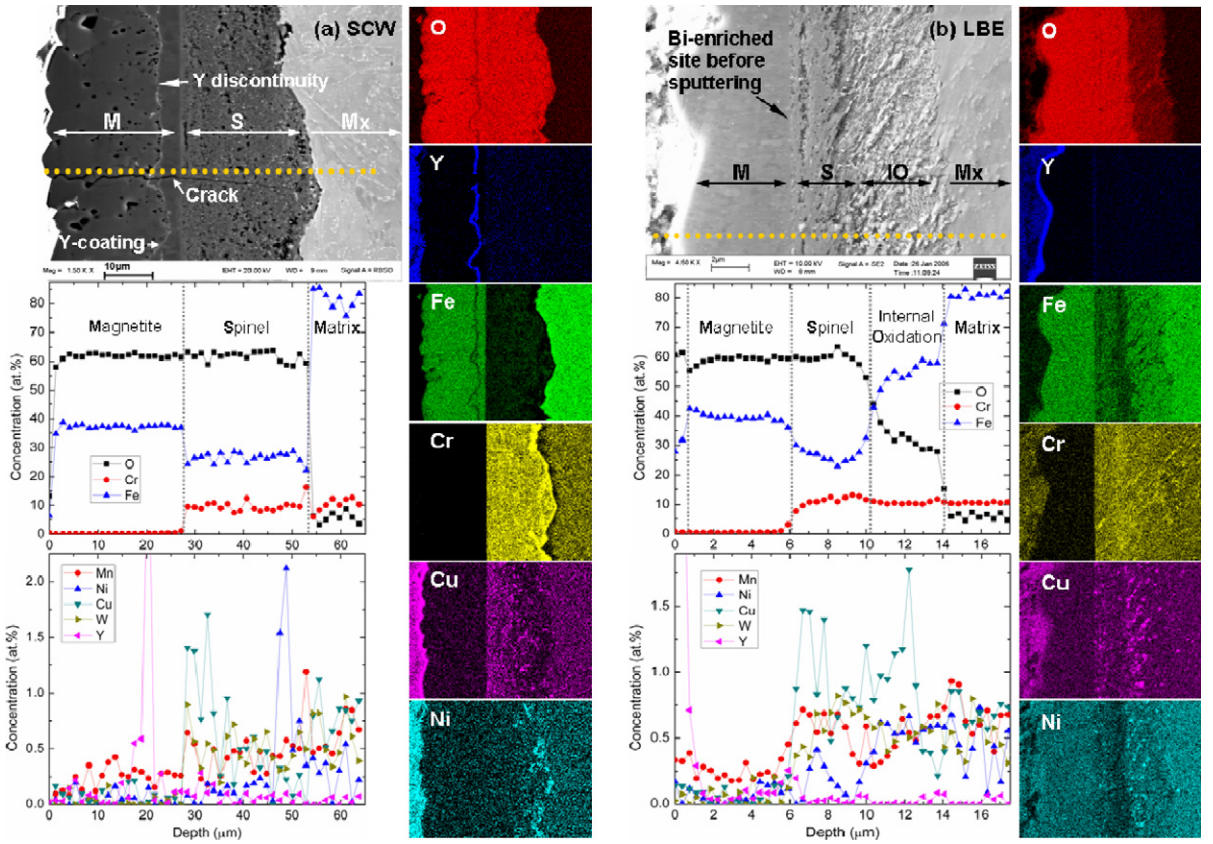


Fig. 4. SEM/EDS results of Y-coated samples exposed in (a) SCW and (b) LBE for 667 and 600 h, respectively. The labels on the SEM images are consistent with those in Fig. 3.

thin inner dense layer (~4 μm). The spinel layer is more complex compared to the magnetite layer. The EDS line-scans indicate that chromium and most of the minor alloying elements stopped in the spinel layer without diffusion into the magnetite. According to the EDS line-scans and maps, Cu, Ni, and Cr are enriched in the spinel layer with Cu close to the spinel–magnetite interface, and Ni and Cr close to the spinel–matrix interface. The Cr-enrichment at the region close to the spinel–matrix interface is consistent with the XRD result ('Y-int2'), where Cr-rich oxide forms, e.g., $Cr_{1.3}Fe_{0.7}O_3$. In addition to the magnetite and the spinel layers, an internal oxidation layer is present at a few regions beneath the spinel layer. The distribution of the internal oxidation layer in Y-coated sample is not as common as that in the as-received sample. Cracks were observed in the oxide scale, which were not stopped by the Y-coating layer. These cracks may be the same as the ones observed at the oxide surface shown earlier in the plan-view SEM images (Fig. 2). The cracks were not observed in our previous study on HCM12A exposed in SCW at 500 °C [9].

The oxide layer structure of the Y-coated sample exposed to LBE is similar to that exposed to SCW but without the outer magnetite sub-layer and with a continuous internal oxidation layer. Based on the results of the effect of the Y-coating layer on the oxide scale on the SCW-exposed sample (Fig. 4(a)) and the effect of LBE on the magnetite layer on the as-received sample (Fig. 3), it could be deduced that there is an outer magnetite sub-layer which was detached into the LBE. The inner magnetite sub-layer having a thickness similar to that formed on the SCW-exposed sample is protected by the Y-coating layer which should be an Y-Fe oxide, e.g., $YFeO_3$, as on the SCW-exposed sample due to the similar oxygen concentration in SCW and LBE, and due to the similarity of the oxide layer structure. The protective effect against corrosion provided by the Y-coating layer is expected to be better than that

provided by the spinel layer on the as-received sample (Fig. 3) due to its higher thermodynamic stability. However, the Y-coating layer is discontinuous at some locations (not shown in Fig. 4(b)). The regions with discontinuous Y are associated with the loss of most of the magnetite layer resulting in the exposure of the spinel layer in a manner similar to the as-received sample exposed to LBE. Optimization of the coating process will likely improve the continuity of the Y-coating layer. Bi-enriched Pb–Bi was observed at some locations close to the interface of the spinel and the magnetite, but the amount is limited as evidenced by the SEM image in Fig. 4(b) which was captured after sputtering with a focused-ion-beam. The Bi-enriched penetration region was also observed by Kondo et al. [16]. The EDS line-scans and maps indicate that the internal oxidation layer is characterized by diminished oxygen compared to the outer oxide scale, and some Fe depletion and Cr enrichment compared to the matrix. The pronounced internal oxidation layer on LBE_exposed samples compared to SCW-exposed samples is believed to be induced by the oxygen partial pressure gradient in the oxide scale, which may be affected by the penetrated LBE, favoring the preferential oxidation of Cr. In addition, the EDS line-scans and maps exhibit the enrichment of Cr and Cu at the regions close to the interfaces of the spinel–magnetite and the spinel–internal oxidation layer, and with stronger enrichment at the later interface. Ni is only enriched at places close to the interface of the spinel–internal oxidation layer. The enrichment locations of these elements are different from those in the oxide scale on the Y-coated sample exposed to SCW.

### 3.5. Grain structure and phase distribution of the oxide (EBSD)

To understand the effects of SCW and LBE on grain structure and phase distribution in the oxide scale, EBSD analyses were performed. Fig. 5 shows the EBSD maps of Y-coated samples exposed in SCW and LBE for 667 and 600 h, respectively. Magnetite and spinel were not differentiated during the EBSD analysis due to their similar crystal structure. As shown in the SCW-exposed sample (Fig. 5(a)), the magnetite layer is divided into two sub-layers by the Y-coating layer identified as $YFeO_3$. The outer magnetite sub-layer is mainly composed of large columnar grains along the growth direction of the oxide scale. The inner magnetite sub-layer is mainly composed of small equiaxed grains as in the spinel layer. A mixture of ferrite and spinel exists at the region close to the interface of the spinel and the matrix. The outer sub-layer of magnetite on the LBE-exposed sample was detached into the LBE. As shown in the EBSD

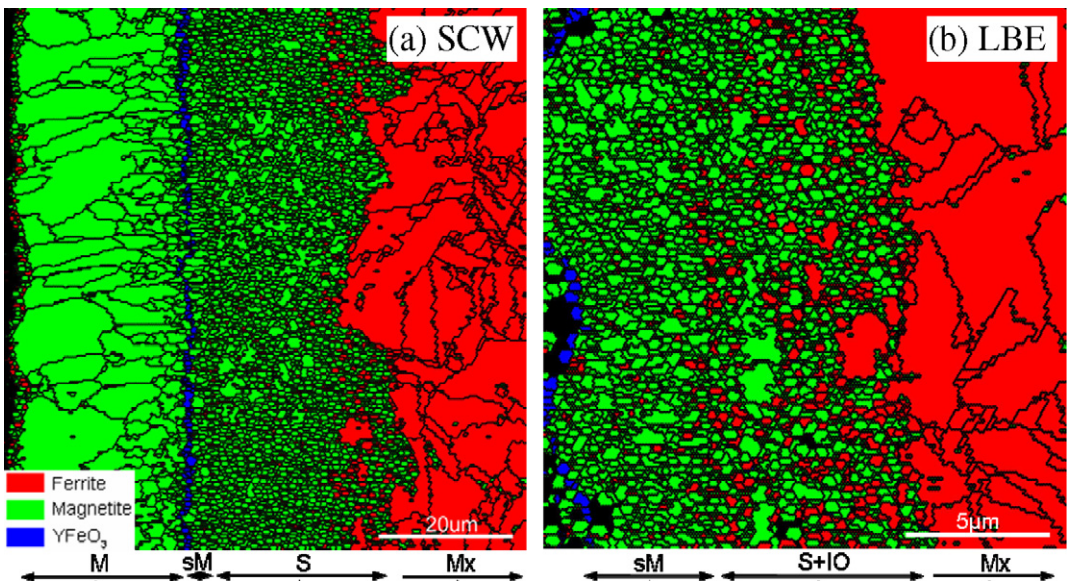


Fig. 5. EBSD maps of Y-coated samples exposed in (a) SCW and (b) LBE for 667 and 600 h, respectively. In addition to the labels as used in Figs. 3 and 4, sM denotes the inner sub-layer of magnetite.

map of the LBE-exposed sample (Fig. 5(b)), some sparse magnetite grains remain in the outer sub-layer. The spinel and internal oxidation layers are mainly composed of spinel phase with some ferrite mixture, especially in the internal oxidation layer.

In addition to the major phases (ferrite, magnetite/spinel, and $YFeO_3$), some trace amounts of phases, e.g., Cu at the magnetite–spinel interface, Ni and $Cr_{1.3}Fe_{0.7}O_3$ at the spinel–matrix interface, and FeO in the internal oxidation layer, were identified in SCW-exposed samples by EBSD spot mode with their locations guided by the EDS maps as shown in Fig. 4. The observation of $Cr_{1.3}Fe_{0.7}O_3$ at the interface of spinel–matrix is consistent with the XRD results ('Y-int2'). Cu and Ni were not oxidized due to the low oxygen partial pressure in the spinel layer, which favored Cr preferential oxidation but not Cu and Ni. The LBE-exposed sample possesses similar observations. According to the Fe–O phase diagram, FeO should form at temperatures above ~570 °C. It has been reported that FeO forms at regions closest to the interface of oxide-matrix on 12%Cr steels exposed in Ar–50%$H_2O$, e.g., 12Cr–Mo–V steel at 550 °C and Fe–12Cr–4Co model alloy at 600 °C [17]. The presence of FeO in the internal oxidation layer in SCW-exposed samples was confirmed by EBSD spot mode. FeO was not observed in LBE-exposed sample due to the lower exposure temperature.

Inverse pole figures (IPF) and texture intensity of the different layers/phases in Fig. 5 are listed in Table 3. The matrix (ferrite) of the samples exposed in SCW and LBE does not show the distinct 1 1 0 texture generally observed in body-centered-cubic materials. For the sample exposed in SCW, 1 1 1 texture emerges with the formation of face-centered-cubic phases, spinel and magnetite. Weak 1 1 1 texture was also observed in the XRD study. Texture becomes diversified from the spinel layer to the outer sub-layer of magnetite with the growth of the oxide scale. The evolution of the texture formed in the sample exposed in LBE is similar to that exposed in SCW. However, distinct 1 1 1 texture does not exist in the spinel and internal oxidation layers for the spinel phase. This is due to the relatively extensive mixture of spinel and ferrite in the internal oxidation layer. The maximum intensity of the textures in different layers/sub-layers indicates that the texture intensity decreases as one proceeds from the matrix (ferrite) to the outer regions of the oxide scale.

Table 3
Inverse pole figures (IPFs) and texture intensity for different layers/phases as shown in Fig. 6

| | SCW | LBE | Texture intensity |
|---|---|---|---|
| Magnetite (outer sub-layer) | 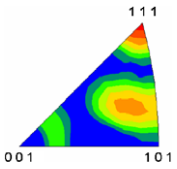 | | 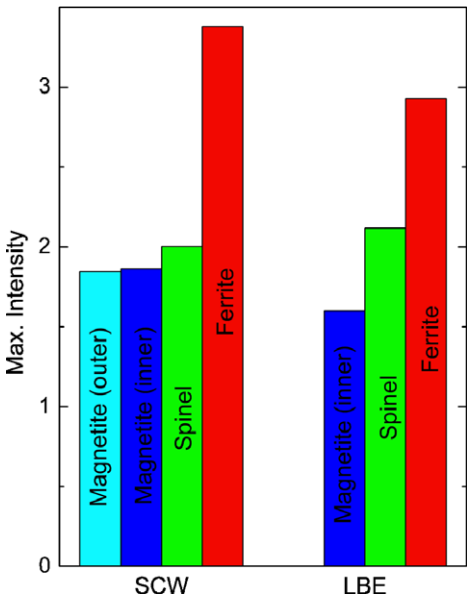 |
| Magnetite (inner sub-layer) | 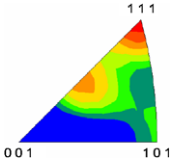 | 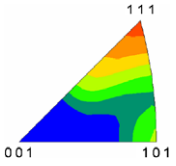 | |
| Spinel/(spinel internal oxidation) | 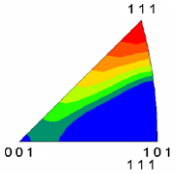 | 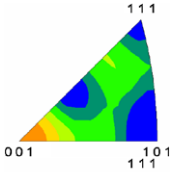 | |
| Matrix | 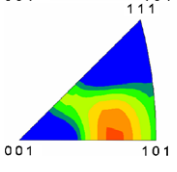 | 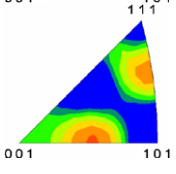 | |

## 4. Conclusions

The corrosion behavior of a 12%Cr ferritic/martensitic steel HCM12A with and without an yttrium surface coating exposed to SCW and LBE was studied by means of gravimetry, XRD, SEM/EDS, and EBSD. The Y-coated sample exposed in SCW demonstrated improved corrosion resistance, as measured by its decreased weight gain and thinner oxide scale compared to the as-received sample.

The oxide scale formed on both SCW- and LBE-exposed samples is mainly composed of a two-layer structure: the outer magnetite and the inner spinel. The magnetite layer is porous compared to the spinel layer. Cracks were observed in the oxide scales formed on both as-received and Y-coated samples exposed to SCW. An internal oxidation layer also exists at the interface of the spinel and the matrix. It is a continuous layer (along the oxide–metal interface) on LBE-exposed samples. On the contrary, the internal oxidation layer on SCW-exposed samples is discontinuous, especially for the Y-coated sample having the smallest internal oxidation layer. The Y-coating layer divides the magnetite layer into two sub-layers: the outer porous thick sub-layer and the inner compact thin sub-layer. The outer magnetite sub-layer is composed of large columnar grains along the oxide scale growth direction. The inner magnetite sub-layer is similar to the spinel layer being composed of small equiaxial grains. One of the major differences between LBE- and SCW-exposed samples is that the outer magnetite layer on LBE-exposed samples was detached into the LBE. The Y-coating layer prevented the inner magnetite sub-layer from detachment, which may be desirable for enhanced corrosion resistance. In addition to the nature of SCW and LBE, the exposure temperature and oxygen partial pressure played an important role on oxide formation.

In addition to the major phases, ferrite, magnetite, and spinel, other phases, such as $YFeO_3$ at the Y-coating layer, and $Cr_{1.3}Fe_{0.7}O_3$ and Ni at the interface of spinel–matrix/internal oxidation layer, were identified by means of XRD and/or EBSD. These observations are consistent with the elemental enrichment, e.g., Cu, Cr, and Ni, at the corresponding locations. FeO was observed in the internal oxidation layer on SCW-exposed samples but not on LBE-exposed samples. Weak 111 texture was observed in the oxide scale. The texture intensity decreased with the growth of the oxide scale.

## Acknowledgements

This work is supported by the Idaho National Laboratory as part of the US DOE Generation IV Initiative and in part supported by the US DOE under the NEER Program Award No. DE-FG07-04ID14600 and NEER Project No. 81.114.

This report was prepared as an account of work sponsored by an agency of the United States Government. Neither the United States Government nor any agency thereof, nor any of their employees, makes any warranty, express or implied, or assumes any information, apparatus, product, or process disclosed, or represents that its use would not infringe privately owned rights. Reference herein to any specific commercial products, process, or service by trade name, trademark, manufacturer, or otherwise does not necessarily constitute or imply its endorsement, recommendation, or favoring by the United States Government or any agency thereof. The views and opinions of authors expressed herein do not necessarily state or reflect those of the United States Government or any agency thereof.

## References

[1] J.R. Weeks, Nucl. Eng. Des. 15 (1971) 363.
[2] F. Gnecco, E. Ricci, C. Bottino, A. Passerone, J. Nucl. Mater. 335 (2004) 185.
[3] R.L. Klueh, D.R. Harries, High-Chromium Ferritic and Martensitic Steels for Nuclear Applications, ASTM International, West Conshohocken PA, 2001, (p. 5) (ISBN: 0-8031-2090-7).
[4] F. Masuyama, New developments in steels for power generation boilers, in: R. Viswanathan, J. Nutting (Eds.), Advanced Heat Resistant Steels for Power Generation, Conference Proceedings, San Sebastian, Spain, 27 April 1998.
[5] R. Viswanathan, W. Bakker, J. Mater. Eng. Perform. 10 (2001) 81.
[6] Z. Klenowicz, K. Darowicki, Corros. Rev. 19 (2001) 467.
[7] I.G. Wright, B.A. Pint, An assessment of the high-temperature oxidation behavior of Fe–Cr steels in water vapor and steam, in: NACE Corrosion, Denver, CO, 8–11 April 2002, paper no. 02377.
[8] S. Osgerby, A. Fry, Stream oxidation of 9–12%Cr martensitic steels: the influence of laboratory practice, in: A. Strang et al. (Eds.), Parsons 2003 Engineering Issues in Turbine Machinary, Power Plant and Renewables, IOM3 2003, p. 295.
[9] L. Tan, Y. Yang, T.R. Allen, Corros. Sci. 48 (2006) 3123.
[10] T. Furukawa, G. Muller, G. Schumacher, A. Weisenburger, A. Heinzel, F. Zimmermann, K. Aoto, J. Nucl. Sci. Technol. 41 (2004) 265.
[11] D.P. Whittle, J. Stringer, Philos. Trans. R. Soc. Lond. A 295 (1980) 309.

[12] K. Sridharan, A. Zillmer, J.R. Licht, T.R. Allen, M.H. Anderson, L. Tan, Corrosion behavior of candidate alloys for supercritical water reactors, in: Proceedings of International Congress on Advances in Nuclear Power Plants (ICAPP 2004), Pittsburgh, PA, 13–17 June 2004, p. 537.
[13] V. Tcharnotskaia, C. Ammermann, K. Woloshun, Results from the initial operation of the LANL DELTA loop, in: The 3rd Workshop Proceedings of Utilisation and Reliability of High Power Proton Accelerators, Santa Fe, NM, 12–16 May 2002, p. 385 (published in 2003).
[14] D.P. Field, Ultramicroscopy 67 (1997) 1.
[15] J.M. Francis, W.H. Whitlow, Corros. Sci. 5 (1965) 701.
[16] M. Kondo, M. Takahashi, T. Suzuki, K. Ishikawa, K. Hata, S. Qiu, H. Sekimoto, J. Nucl. Mater. 343 (2005) 349.
[17] J. Zurek, L. Nieto Hierro, J. Piron-Abellan, L. Niewolak, L. Singheiser, W.J. Quadakkers, Mater. Sci. Forum 461–464 (2004) 791.